Optimal Angle in Bistatic Measurement for Chipless Tag Detection Improvement

Raymundo de Amorim Junior, Romain Siragusa, Nicolas Barbot, Etienne Perret

Optimal Angle in bistatic Measurement for Chipless Tag Detection Improvement

Raymundo de Amorim Jr, Romain Siragusa, Nicolas Barbot *Member, IEEE*, Etienne Perret, *Senior Member, IEEE*

***Abstract*—This paper shows the use of a bistatic reading configuration by optimizing the angle between the two antennas that allows isolating the contribution of the RFID chipless tag from its nearby environment, thus enhancing the reading performance of the chipless tag for short-range applications. The idea is to extract as much useful signal (relating to the tag information or tag ID) from the total signal using a dedicated bistatic reading configuration. This extraction step is implemented from a hardware point of view, which is different from classical approaches based on signal processing. Indeed, based on this technique, it is possible to read tags even in highly reflective environments (metallic surfaces) without applying a calibration method, such as subtracting the environment without the tag or advanced post-processing steps. For this purpose, a bistatic antenna configuration is employed, where the angle between the incident wave and the backscattered signal is chosen to maximize co-polarization configuration. Firstly, a model based on the general scatter theory is evaluated; it highlights the scattering mechanism involved in the problem. Then, a proof of concept (PoC) is evaluated, and afterward, a chipless tag composed of an array of dipoles is studied for identification purposes. The analytical evaluation and the channel modeling allow a general implementation of the proposed technique. Anechoic and real scenario measurements are evaluated considering the presence of surrounding objects. Finally, non-systematic errors related to the positioning of the tag are considered each time without considering a reference (or background) measurement or the use of specific signal processing techniques.**

***Index Terms*—Chipless RF identification (RFID), detection reliability, frequency-domain reading method, bistatic measurement, scattering pattern.**

I. Introduction

THE needs for identifying and capturing physical information are among the main matters in modern societies. Radio Frequency IDentification (RFID) is one of the major technologies that has been experiencing considerable growth in the identification field. This technique automatically retrieve information by remote reading. RFID tags can be classified according to their power supply, operating frequency, cryptographic capacity and communication protocol, or even by the presence or not of an electronic chip [1]. Among the RFID systems, the UHF-RFID has experienced a wide implementation, each tag is composed by an antenna that backscatters a signal modulated by a chip. In terms of costs, the chip represents the costly part of the UHF-RFID tag fabrication. Thus, the chipless technology is employed as a cost reduction alternative [1].

Chipless tags can be seen as radar targets designed to scatter a specific electromagnetic signature [1]. Consequently, the coded information in chipless systems is directly related to the geometry of the metallic patterns that comprise the tag. The reader transmits a Radio Frequency (RF) interrogation signal towards the tag, which generates currents on the metallic elements, and after, the reader captures the backscattered signal. Two main families of tags can be distinguished according to the technique used to code the information: time domain tags [2]–[4] and frequency domain tags [5]–[7]. Time coding tags work based on a reflectometry principle; the tag usually consists of a transmission line connected to one or two antennas. Discontinuities can be positioned along the line to create reflections or delays, where each echo positions determines the coding information [2], [3], [8]. Time-Coded UWB chipless RFID tags may achieve a few meters in reading range. However, time-coded tags do not guarantee to encode sufficient bits within a credit card-sized area. Therefore, time domain-based tags cannot attend to a high data encoding density. In the frequency coding-based tag, the tag's resonant patterns show dips/peaks in the spectrum of the backscattered signal. Therefore, retrieving the tag ID consists in precisely determining the frequencies at which these dips/peaks occurred. Frequency-based tags can encode more information considering a credit card size area, which is closest to the needs for identification purposes. Then in the following, only frequency-based tags will be considered.

One of the main challenges for chipless RFID systems is the reading robustness; several techniques attempt to reliably retrieve the tag ID from the clutter signal captured in real environment [9]–[15]. These techniques comprises polarization diversity, time domain techniques, and image-based system. These techniques attempt to enhance the tag signal over the clutter contributions, that arises from peripheral objects and coexistent inference sources.

This article presents a calibration-free technique based on bistatic measurement for chipless tag reading for the first time. The proposed technique exploits the angle between the reader antennas in a bistatic configuration. By correctly choosing this angle, it is possible to remove the quasi-optic mode from the backscattered signal. Unlike other approaches, this one is promising, considering high reflective scenarios. Consequently, theoretical analysis, simulation, and measurement of

This work was supported by the project AUSTRALE via Agence Nationale de Recherche. (Corresponding author: Raymundo de Amorim Junior.).

The authors are with the Laboratoire de Conception et d'Intégration des Systèmes (LCIS), Grenoble Institute of Technology (Grenoble-INP),Valence 26000, France, (e-mail: raymundo.de-amorim-junior@lcis.grenoble-inp.fr; romain.siragusa@lcis.grenoble-inp.fr; nicolas.barbot@lcis.grenoble-inp.fr)

E. Perret is with the Laboratoire de Conception et d'Intégrationdes Systèmes (LCIS), Grenoble Institute of Technology (Grenoble-INP), Valence 26000, France, and also with the Institut Universitaire de France, Paris 75005, France, (e-mail: etienne.perret@lcis.grenoble-inp.fr).

the far-field scattering patterns for a single dipole aiming the PoC is done. Afterward, the study of an array of dipoles is presented for identification purposes. This approach can be interpreted as a hardware technique (like cross-polarization reading in chipless) that is added to other classical reading techniques already implemented. Moreover, it allows taking a new step towards chipless tag reading in constrained environments for real applications.

The state of the art techniques is addressed in Section II. Then channel modeling opens up the implementation for general applications in Section III. In Section IV and Section V, the anechoic setup is presented, and measurements in the presence of objects are performed, and in Section VI, the measurements are performed in a real scenario, considering several reflective objects. Section VII assesses the impact in real reading situations and its limitations. Finally, Section VIII evaluates a metric based on the decoding capability.

II. Frequency-domain measurement methods for chipless tags reading

The classical method used to extract the tag response from the environment relies on subtracting two different measurements: one with the tag and another without the tag presence. This technique is the simplest calibration technique to implement and can be performed while the environment stays unchanged. Therefore, it significantly reduces a part of the different reflections involved in the measurements (the antenna mismatch or coupling, part of the wave directly reflected by the objects positioned in front of the antenna…) [6], [16], [17]. Nonetheless, the method can be performed if the environment is not modified in-between the two measurements (static environment).

High gain and narrow beam antenna arrays have been discussed in reflect-arrays as examined in [14], [15]. Indeed, the high directive beam isolates the tag from the nearby contributions. However, consider RF barcodes that have the usual distance reading of around a meter, size limited to a credit card, and add the regulation issues (UWB). Therefore, these constraints make it impractical to increase the gain of the tags (especially as in [15] by using antenna array structures) or on the reader side to use even larger gain antennas than those to UWB.

Nowadays, three main axes are implemented for robust detection and will be discussed in the rest of this Section: polarization diversity, time domain techniques, and image-based system.

A. Polarization diversity

In the context of chipless RFID, polarization diversity relates to the polarization dependencies between the tag and the reader antennas. In this sense, the resonators can depolarize a part of the incident wave to respond perpendicularly to the polarization of the incident wave [9]. Therefore, higher isolation between the emitted and the backscattered waves is obtained, and the clutter reflections from surrounding objects can be reduced. However, the most common objects (cardboard, plates, etc...) do not have a natural tendency to depolarize the incident wave (like resonant scatters), so the depolarizing effect mainly concerns the signal part that contains the ID. Indeed, a backscattered signal with polarization orthogonal to that of the incident wave can be generated by a resonant element having, for example, an asymmetry concerning the incident wave. The proposed structure in [9] is composed of a set of short-circuited half-wave dipoles backed by a ground plane. Contrarily to the resonant element that comprises the tag, the ground plane, when aligned with the incident field, like most common objects, does not depolarize the incident wave. However, without post-processing, the calibration of the background environment is needed.

Another approach based on two co-polarization measurements has also been introduced to improve chipless tag reading in real environments. First, specific tags have been introduced where the ID is coded in the difference between the vertically and horizontally polarized backscattered waves [10]. Indeed, two reflection coefficient measurements should be performed simultaneously in vertical and horizontal polarization when the tag is correctly aligned. Then, the recorded responses on the two channels are filtered in the time domain and subtracted in the frequency domain. Finally, chipless tag readings using circular waves were also reported in the literature [11]. Circular polarization is exploited to isolate the field scattered by the tag from that of surrounding objects. However, the reader polarization diversity significantly increases the complexity and cost associated with the chipless implementation system.

B. Time gating

Post-processing techniques are a different way to increase the ratio between the resonant and the quasi-optic mode, *i.e.*, the resonant-to-quasi-optic mode. This is undoubtedly the simplest and, therefore, the most effective approach to implement since, unlike those described above, no hardware modification is required. Different post-processing techniques are used in chipless RFID systems aiming to read the tag with only one measurement, *i.e.*, without any calibration. The reader retrieves the tag backscattered signal; thus, post-processing is applied. A usual way to partially remove the clutter or resonant contributions is to perform time gating [18]. A time window is positioned after the first strong peak due to the tag quasi-optic mode until the known last resonant time (a few dozen nanoseconds). Indeed the early-time corresponds to the part of the signal where the specular reflection is significant and must be removed. Conversely, the late-time corresponds to the signal part that mainly includes the tag ID. However, the filtering process does not remove any other contribution that is located temporarily between the beginning and the end of this window (for instance, a reflection by an object located a few tens of centimeters beyond the tag). Despite the problems, this technique is widely used for its simplicity and suitability.

This method can also be combined with other advanced post-processing approaches such as Short-Time Matrix Pencil Method [12] or Short-Time Fourier Transform [13], [19]. The main principle is applying a sliding window to the temporal signal to recover the tags' resonance frequencies. The methods presented in [12] and [19] allow to extract aspect-independent

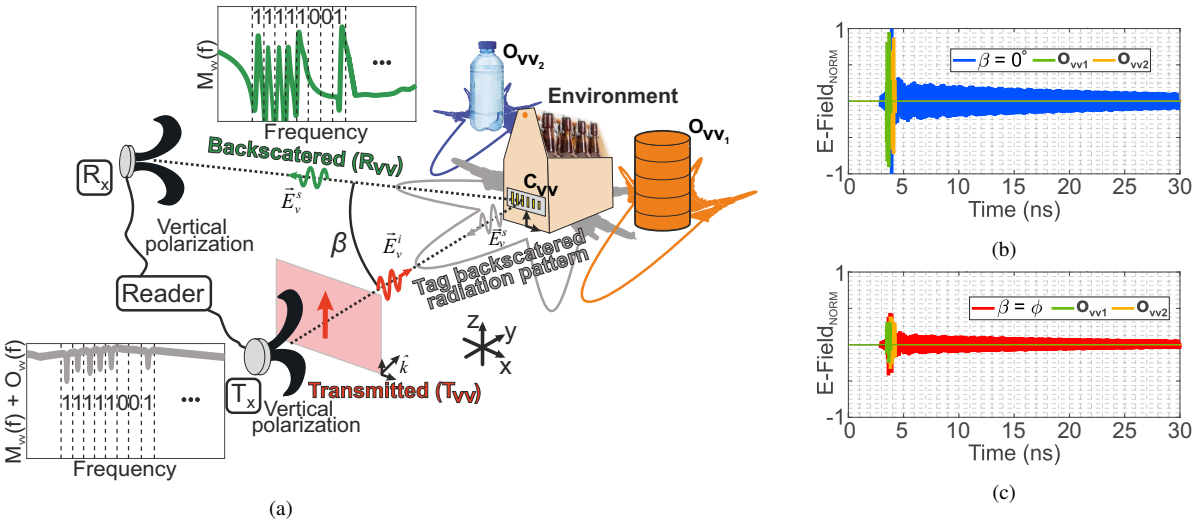

Fig. 1: (a) Scheme of the bistatic measurement of a chipless RFID system considering the different signals and polarization concerned, (b) time-domain signal at $\beta = 0°$, and (c) time-domain response at $\beta = \phi$.

parameters (that are analogous to complex natural resonances) of chipless RFID tags. Generally, the extraction of the resonant frequencies consists in determining maximums (peak apexes) on the frequency representation of the signal backscattered by the tag. These frequencies thus extracted may not correspond precisely to the resonance frequencies, in particular, because of the presence of the quasi-optic mode in the backscattered signal, which can affect the peaks present on the frequency representation of the signal. The possibility to implement techniques giving access to aspect-independent parameters allows to improve the reading of tags in unknown environments and potentially without calibration measurements [19]. In addition, the extraction of the quality factor of each resonance frequency is used to improve tag ID detection by reducing false readings [19]. Indeed, it has been shown that the desired peak apexes corresponding to the ID can be separated from spurious peak apexes.

However, eliminating the early-time part of the signal has negative effects. Reducing the duration of the signal will reduce the frequency resolution, which in chipless results in reducing the amount of information contained in the tag. In the same way, this removed temporal part still contains some useful signal from the tag, which will not be used for decoding. This last point becomes even more damaging when the resonance frequencies increase: the quality factors decrease as well as the duration of the temporal signal relative to the resonance. Furthermore, another drawback of time gating relates to the determination of the time window, *i.e.*, the beginning time and the ending time. This requires at least information about the tags to be read, for example, the quality factors of the resonators forming the tag.

However, time gating remains very simple to implement and can be combined with other techniques, such as those related to measurement methods.

C. Image-based system

Image-based systems have been exploited in chipless RFID systems for more than ten years. It is one of the first techniques implemented to design a chipless RFID system [20].

The idea is to encode information with the position and orientation of the conductive patterns that make up the label. The chipless image-based systems combine a specific measurement technique similar to a synthetic aperture radar (SAR) with a dedicated post-processing step. In [21], a dual-polarized resonant reader retrieves the information from depolarizing tags by combining a SAR image processing algorithm. The retrieved cross-polarized signal enables the clutter contributions suppression. In [22], a set of geometric structures with different polarimetric backscattering behaviors are analyzed to operate like chipless tags. The information is obtained by the structure's polarization diversity of the signal backscattered. However, a calibration process is carried out. The main drawback of image-based systems is the high complexity of the reader hardware and interrogation process, thus losing the cheap proposition of the chipless RFID-based systems. Millimeter waves are preferred to implement the SAR approach while having an antenna array and tag dimensions compatible with the application.

III. Bistatic Measurement Approach

A. Working principle

The backscattering mechanism of the chipless tag can be divided into two contributions: the quasi-optic mode or structural mode and the resonant mode [1]. When an incident signal impinges the tag, the structure directly reflects a portion of the power following a quasi-optic reflection. The clutter signals and antenna coupling are embedded in that signal. The second part of the signal is the resonant mode, which contains the EM chipless tag information. The chipless tag EM's response combines a resonant mode (relating to the ID) and the quasi-optic mode.

Since the information is only coded into the resonant mode of the tag response, any superimposition of the quasi-optic mode and clutter collaborations over the resonant mode is a problem for tag detection since peaks in the frequency spectrum are overlapped by the clutter signal level [19]. In this way, it is known that the tag reading robustness is significantly affected by the signal-to-noise ratio (SNR) of the received backscattered signal or, specifically, the resonant to quasi-optic mode ratio (RQMR). One way to improve the RQMR is to choose a reading at an angle β using a bistatic co-polarization configuration from which the RQMR improves considerably. β expresses the bistatic angle between the transmission and reception antenna. Indeed, when the tag is located in the plane perpendicular to the incident wave, quasi-optic reflections are backscattered in the same direction of the excitation, contrary to the resonant mode that will be backscattered in different directions that could be the specific direction β. The backscattered pattern can be established at the resonance frequencies of the analyzed tag as a function of the bistatic angle β.

Fig. 1(a) shows a scheme of the bistatic measurement of a chipless RFID system considering the signals and polarization under concerned. The reader transmits a wide-band vertically polarized signal that impinges the tag, and then, at a β-angle the vertically polarized antenna retrieves the backscattered signals. As depicted in Fig. 1(a), the arrow toward the R_x indicates the portion of the received backscattered signal. At $\beta = 0°$ the incoming signal mostly comprises quasi-optic backscattered responses from the objects and the tag. Meanwhile, at $\beta = \phi$, the quasi-optic reflections are drastically decreased. Thus the majority of the received signal is from the resonant mode. Therefore, it is clear that the relationship between the resonant and the quasi-optic modes can be improved due to the bistatic angle. Fig. 1(b) details the co-polarized signals in the time domain for $\beta = 0°$, which corresponds to the classical case, the early-time response presents high clutter reflections and the quasi-optic tag reflection. The non-zero angle (ϕ), Fig. 1(c), represents the improved tag response compared to the clutter and quasi-optic reflections. The tag response (C_{vv}) is given for these two angles. We can see that the signal scattered by the objects $(O_{vvi}; i = [1, 2])$ constitutes the main part of the signal received by the reader (M_{vv}) when $\beta = 0°$ is considered. A quasi-optic level reduction regarding a hypothetical angle (ϕ) can be observed if we compare the received signal at two angles [Fig. 1(c)]. Therefore, considering specific directions $(\beta \neq 0)$, the resonant mode can be predominant over the quasi-optic mode.

To implement such a technique, the objective is to find a bistatic angle β between the *a priori* known incident wave and the received antenna that maximizes the ratio between the resonant and the quasi-optic mode.

B. Channel modelling

The channel model block diagram was analyzed in [9] to characterize the isolation between a depolarizing chipless tag and the surrounding environment. After that, a channel model is presented in [13], to highlight the time dependence between a tag composed of resonant elements and the surrounding environment. Finally, the block diagram that exemplifies the quantities concerned in the problem is depicted in Fig. 2. To include the dependence of the angle (β) between the transmission and reception antennas in the model, all the coefficients of each block (2×2 matrix) introduced in Fig. 2 are a function of β.

Then, with the same derivation done in [9], the signal retrieved in co-polarization by the reader M_{vv} is:

$$M_{vv} = [C_{vv}(\beta) + O_{vv}(\beta)]R_{vv}(\beta)T_{vv}(\beta) \tag{1}$$

Note that some assumptions have been made to obtain (1). For example, the surrounding objects are considered to not depolarize the signal, thus their horizontal and cross-polarization terms $(R_{vh}, C_{vh}, C_{hv}, C_{hh}, T_{hv}, O_{hv}, O_{vh}, O_{hh})$ have been neglecting. Also, in bistatic measurements the isolation measurement (noted *I* in [9]) tends to zero.

The tag response in co-polarization (C_{vv}) can also be represented considering the resonant and the quasi-optic mode. Therefore, the term (C_{vv}) can be rewritten, following $C_{vv}(\beta) = c^{st}_{vv}(\beta) + c^{res}_{vv}(\beta)$. The superscript "$st$" and "$an$" denote the tag's quasi-optic and resonant modes, respectively. Note that for classical resonant scatters like the ones used here, c^{res}_{vv} can be modeled as a second-order resonator [19].

Note also that if for a given non-zero angle β, we have the relations $c^{res}_{vv}(\beta) \gg O_{vv}(\beta)$ and $c^{res}_{vv}(\beta) \gg c^{st}_{vv}(\beta)$ the terms O_{vv} and c^{st}_{vv} can be neglected, and the following relation can be considered:

$$M_{vv}(\beta) = c^{res}_{vv}(\beta)R_{vv}(\beta)T_{vv}(\beta) \tag{2}$$

Then, the received co-polarization response (M_{vv}) is the only function of the tag ID response and of the $(R_{vv}(\beta); T_{vv}(\beta))$ term, which do not depend from the surrounding environment of the tag. In the next section, simulations are performed to assert the model robustness and to find the angles β for which is possible to consider the assumption $c^{res}_{vv}(\beta) \gg O_{vv}(\beta)$. Note that (2) is similar to [[9], Eq. (9)] which is also independent from the presence of any object with the difference in the fact that [[9], Eq. (9)] corresponds to the signal retrieved in cross-polarization for a depolarizing tag.

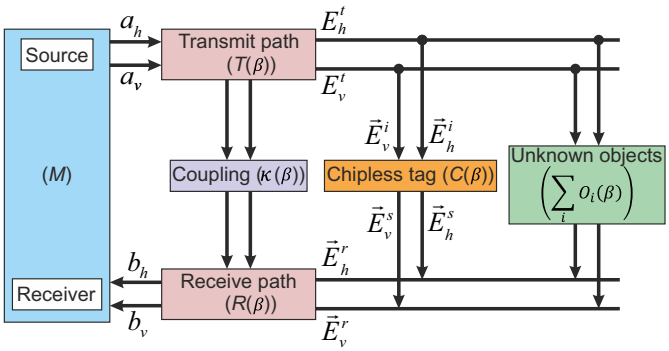

Fig. 2: Channel model system based on the angle (β) between the transmission and reception antennas.

C. Analytical formulation

The model introduced here is based on the idea that our resonators are open circuit patch antennas (or open circuit microstrip dipole). Also, it is possible to use the well-known formalization describing the radiated field of an antenna. Indeed, the scattering properties of any antenna can be characterized by obtaining the values of the radiation properties and the structural scattering of the antenna. The field scattered by an antenna as a function of the load impedance is given by in the following expression [23],

$$E_s(Z_L) = E_0 + \frac{Z_L}{Z_L\, Z_A}\frac{I_0}{I_a}E_r\,. \tag{3}$$

Where $E_s(Z_L)$ is the total scattered field when the antenna is terminated with the load Z_L. E_0 and I_0 are respectively the scattered fields and the short circuit current when the receiving antenna is terminated with a short circuit ($Z_L = 0$). In Eq. 3, Z_A corresponds to the antenna impedance. E_r corresponds to the field radiated by the antenna with a current I_a at its input. Note that the first term relies on a quasi-optic backscattering phenomenon and the second term on the antenna behaviors (sometimes known as the resonant mode), which in our case is a resonant device (patch antenna). From that equation, we have a clear separation between the quantities involved in the problem, which yields the total scattered field E_s.

The quasi-optic term is strictly related to the incident field, the surrounding objects that compose the measurement environment, and the substrate on which the tag is built. Considering a microstrip dipole, the quasi-optic term is obtained by short-circuiting the dipole with the ground plane $(0.3\lambda \times 1.2\lambda)$, which corresponds to the field backscattered by a rectangular plate. In this sense, the short-circuited dipole doesn't interact with the incident plane wave. It is important to note that the co-polarized received scattered field is retrieved according to the largest ground plane dimension.

As mentioned earlier, our tag (particularly when it has a single resonator) is an open circuit patch antenna, *i.e.* $Z_L \to \infty$. Thus, we can rewrite Eq. 3 considering the previous assumptions leading,

$$E_s = E_0 + \frac{I_0}{I_a}E_r\,. \tag{4}$$

We note that the terms E_s and E_0 are backscattered fields (they are excited by an incident plane wave on the structure, in this case, in simulation, the excitation is imposed in $\mathrm{V/m}$) while E_r is a field radiated when we place a port at the antenna (in the case with port giving access to the S-parameters, we can impose 1 W for example, we can also excite the structure with a current source and impose for example $I_a = 1$ A). The fact that these two quantities are related to different types of excitation explains the presence of the term I_0/I_a, which allows considering this essential aspect. This ratio I_0/I_a is a constant independent of the observation angles and will be obtained in simulation to allow us to use Eq. 3 to explain the introduced approach.

Considering the microstrip dipole, the quasi-optic term is obtained by short-circuiting the dipole with the ground plane $(0.3\lambda{\times}1.2\lambda)$, which can be approximated to the field backscattered by a rectangular plate of dimension $(0.3\lambda \times 1.2\lambda)$. In this sense, the short-circuited dipole doesn't interact with the incident plane wave. Therefore, it allows applying for E_0 the analytical expression of the backscattered field of a metal plate [24]. This hypothesis has been verified in simulation and measurement.

It is important to note that the metal plate's backscattered field is all the more valid as the dimension of the plate is large compared to the wavelength. In the case of our tag and thus of a ground plane of dimension $(0.3\lambda \times 1.2\lambda)$, the introduced error is not negligible, which led us to compensate for it by multiplying E_0 by a complex constant coefficient to obtain an excelent approximation with the ground plane simulated on CST. Henceforth, that coefficient is considered.

In Eq. (4), the term relating to the antenna radiation pattern E_r, which describes the resonant behavior of our tag, is obtained by assuming the emitted field by a patch antenna along the resonant dimension. Thus, E_r expresses the field radiated by a patch antenna [24].

Each field quantity can be analytically calculated from the clear separation given by Eq. (4).

Note that both fields E_0 and E_r are considered at a far-field distance. The total scattered field (E_s) of the tag (one resonator case) is retrieved from Eq. (4). Full-wave simulation with CST and analytical expressions results are shown in Fig. 3.

From electromagnetic simulations performed using a full-wave simulator, a current ratio $I_0/I_a = 1.4860 - 0.9702i$ is obtained. In addition, it is used to consider the two types of excitation of the quantities present in Eq. 4. First, it corrects the difference in amplitude that we can see between the curves concerning E_r. After this correction, the E_s field is evaluated by Eq. 3 and is similar to the one directly obtained by simulation.

The great interest of Eq. 4 is that this equation allows to link with the channel model system introduced in Fig. 2. Indeed, according to what has been mentioned previously, the term E_r

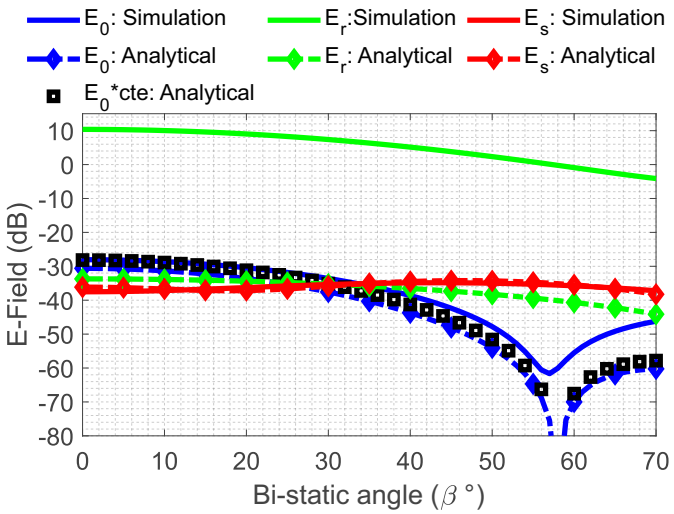

Fig. 3: The simulated and calculated electric fields in bistatic configuration of our tag (one microstrip dipole case).

corresponds precisely to the resonant behavior of the structure and is, therefore, proportional to $c_{vv}^{res}(\beta)$.

As for $c_{vv}^{st}(\beta)$, it is related to E_0, *i.e.*, the specular reflection of the object. $c_{vv}^{st}(\beta)$ is however more general than E_0. Indeed, this term considers all the quasi-optic reflections of the scene.

So, for n objects surrounding the tag we have,

$$c_{vv}^{st}(\beta) \propto E_0(\beta) + O_{vv_1}(\beta) + \cdots + O_{vv_n}(\beta)\,. \qquad (5)$$

We can specify here the different assumptions taken into consideration that will allow us to remove as much as possible the contribution of $c_{vv}^{st}(\beta)$ resulting in the same assumptions that have been done in the Section III-B, *i.e.*, $c_{vv}^{res}(\beta) \gg c_{vv}^{st}(\beta)$.

We should note that the ground plane related to the term $E_0(\beta)$ is a very specific object for a chipless tag reading scene. Indeed, it is a metallic object, flat, relatively small concerning the wavelength, and positioned at normal incidence to the main antenna beam. It can be considered to behave in a very different way from other $O_{vv_n}(\beta)$ objects commonly present in a chipless tag readout scene. Indeed, these objects are generally larger than the tag and can be non-metallic. By considering large objects (metallic or not) placed in normal incidence for the emitted field, we know that they have specular radiation. Therefore the more we deviate from the normal incidence for the reception of the backscattered field, the weaker their contribution will be. Thus, by looking for the value of the angle β_{opt} that minimizes $E_0(\beta)$, we will reduce the contribution of the term $c_{vv}^{st}(\beta)$ and get closer to condition $c_{vv}^{res}(\beta) \gg c_{vv}^{st}(\beta)$. It should be noted that condition $c_{vv}^{res}(\beta) \gg c_{vv}^{st}(\beta)$ is difficult to achieve whatever the environment (we will always find environments incompatible with $c_{vv}^{res}(\beta) \gg c_{vv}^{st}(\beta)$) or even over the entire frequency band considered, however, the bistatic measurement with an optimized angle β_{opt} as described here will reduce the contribution of the environment objects, and better reading for many environments that we encounter in practice will be obtained. This practical validation on real environments will be done based on measurements next sections.

We note that using this model and this approach makes it possible to accurately estimate the angle β_{opt} in the absence of objects.

In Fig. 3, we observe the maximum RQMR around β_{opt} which proves the maximum difference in amplitude between the structural and the scattered resonance contribution. This angle maximizes the RQMR. In other words, the other contributions, namely the quasi-optic reflections, are filtered at that angle.

The results plotted in Fig. 3 are compatible with the assumption done in the paper (in Section III-B) with $c_{vv}^{res}(\beta) \gg c_{vv}^{st}(\beta)$ when β is around $56°$.

Indeed, based on Eq. 4, the linear polarized backscattered electric field as function of the bistatic angle presents the maximum RQMR at $\beta = 56°$. Indeed, the resonant mode represents omni-directional pattern, meanwhile, the quasi-optic pattern has a dip, which determine the bistatic angle that optimize the RQMR. Therefore, the maximum RQMR is determined by the $E_0(\beta)$ behavior, which implies to evaluate

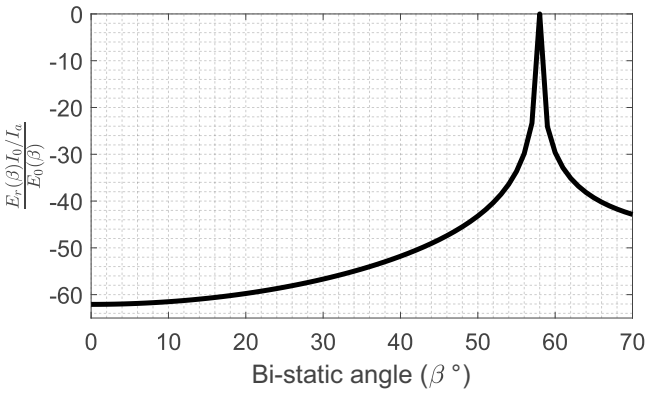

Fig. 4: Normalized resonant to structural mode after the fields corrections.

$\max\left(\dfrac{E_r(\beta)I_0/I_a}{E_0(\beta)}\right)$, the Fig. 4 illustrate the ratio among the antenna and quasi-optic mode as β function. The term $(E_r(\beta)I_0/I_a$ at the resonance condition may be approximated to a constant, which yields in find the minimum contribution of $E_0(\beta)$, *i.e.*, we must determine the angle β corresponding to $\max\left(\dfrac{cte}{E_0(\beta)}\right)$.

D. Proof of concept using full wave EM simulator

A proof of concept based on a simple dipole resonator with a ground plane, which is shown in Fig. 5(a), has been simulated. This dipole length and width are respectively $L_{dip} = 19.8$ mm, and $W_{dip} = 1.5$ mm. The substrate is a Rogers 4003C with relative permittivity $\epsilon_r = 3.38$ and loss tangent $\tan\delta = 0.0027$ with a thickness of 0.81 mm. A ground plane of dimensions $L = 25$ mm and $W = 70$ mm is used. A flat cardboard-based object ($\epsilon_r = 1.78,\ \tan\delta = 0.0025$) has been introduced in the simulation. The tag is placed on an object with larger dimensions than the tag. A plane wave perpendicular to the tag is applied in the simulation. The receiving antenna corresponding to an E-field probe in the solver is positioned with an angle β as shown in Fig.1. At the tag's resonance frequency $(4.46$ GHz$)$, the backscattered radiation pattern (for each β angle) of the object with and without the tag is shown in Fig. 5(a). The maximum difference in amplitude between the two signals (with and without the tag) is obtained when $\beta = 56°$. This angle maximizes the RQMR. The resonant mode dominance is depicted in Fig. 5(b) by the presence of a peak in the frequency response. Indeed, when $\beta = 56°$ a peak prominence around 18 dB is noticed, meanwhile when $\beta = 0°$ the frequency response presents a flat behavior, which reflects the dominance of the quasi-optic mode over the resonant mode.

In Fig. 5(b), for $\beta = 56°$ we observe a characteristic form of a second-order resonator which proves that in this configuration only the resonant mode is recovered by the E-field probe and therefore (2) can be considered. In other words, the other contributions, namely the quasi-optic reflections, are filtered in this reading configuration.

Note that when $\beta = 56°$, the level difference with and without the tag is higher than 20 dB. The object backscattered

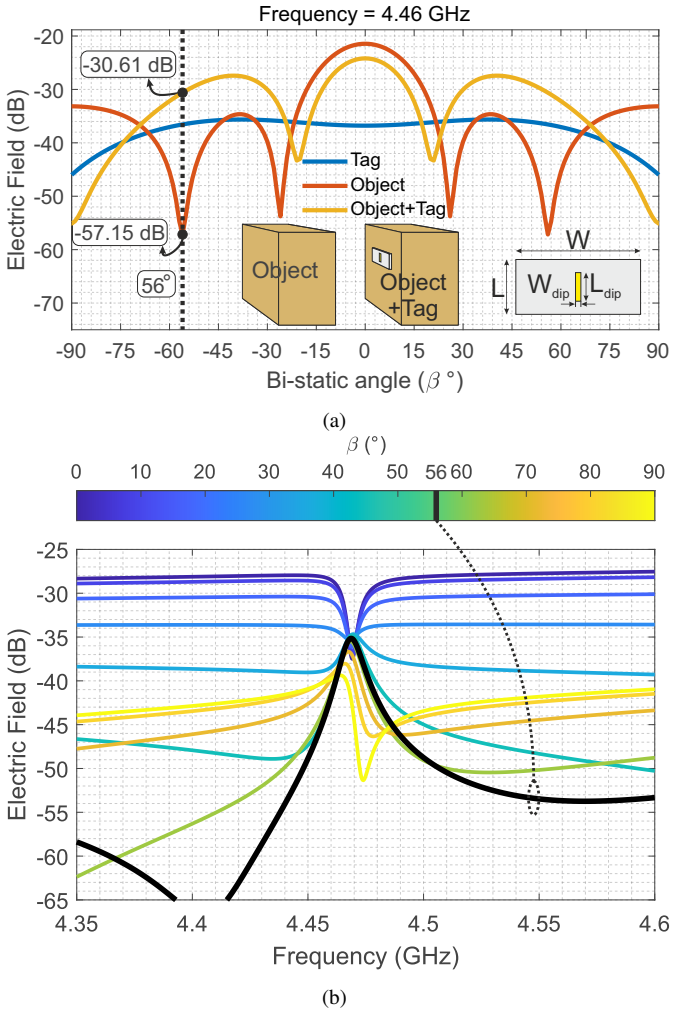

(a)

(b)

Fig. 5: (a) The backscattered pattern as function of β at 4.46 GHz. The incident angle is on direct line-of-sight. (b) Backscattered E-field versus frequency at different β-angles.

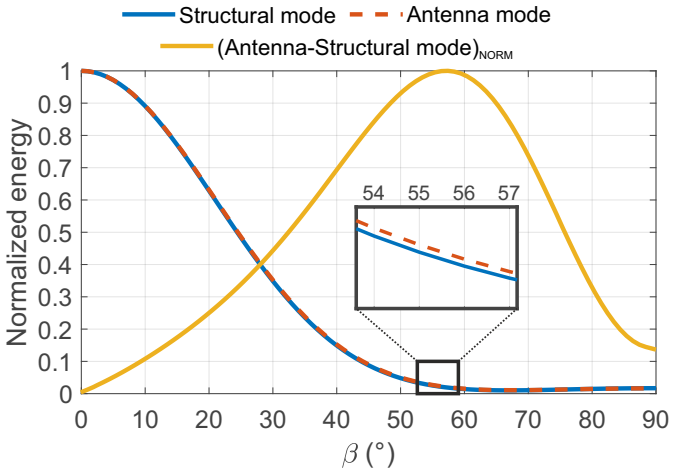

Fig. 6: Characterization of the resonant and quasi-optic mode energy as a function of the bistatic angle (β).

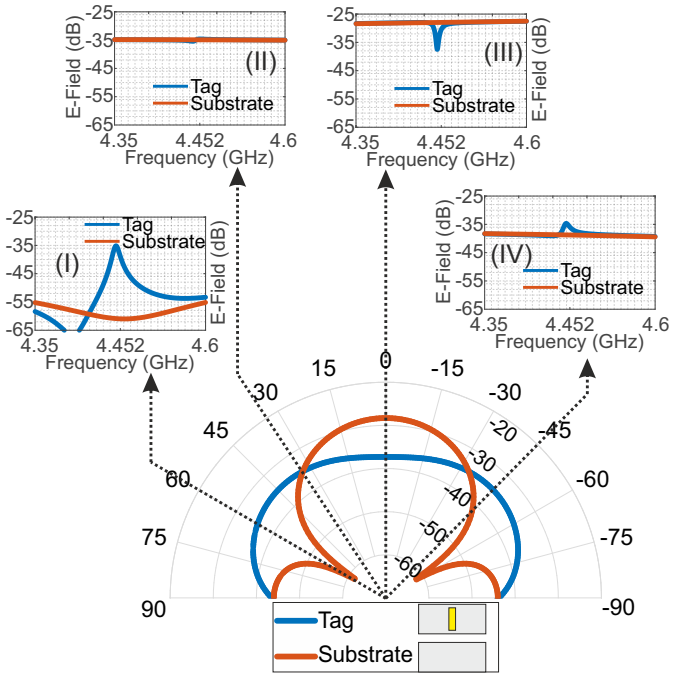

Fig. 7: Co-polarization radiation pattern and frequency response at specific angles.

diagram shown in Fig. 5(a) expresses the tendency to reflect the field in $\beta = 0°$ direction, where the quasi-optic mode is evidenced by a rapid variation around $\beta = 0°$, it is important to note that $\beta = 0°$ direction is much sensible to clutter signals.

To demonstrate the backscattering mechanism and the angle choice criterion based on RQMR maximization, the energy of quasi-optic and resonant modes is evaluated based on their time representation. The quasi-optic mode response is extracted from the substrate backed by the ground plane on time domain simulation. Meanwhile, the resonant mode is calculated by the subtraction between the backed dipole temporal response and the quasi-optic mode. Fig. 6 illustrates the interaction among the resonant and quasi-optic mode energy; at $\beta = 56°$, the difference between resonant and quasi-optic mode represents the maximum ratio. This represents the best angle to recover the tag ID considering the diversity created by the bistatic angle.

On the other hand, multiple angles β can be visualized in Fig. 7 with their respective frequency response. These angles illustrate the different possible configurations: (I) at $\beta \approx 60°$ the RQMR is maximum, then the resonant mode predominance is explicit by the peak on frequency response, which means less influence by the clutter signals; (II) at $\beta \approx 32°$ the amplitude level of the tag and substrate signals are the same, which represents a flat response; (III) the substrate signal is higher than the tag signal; thus a dip is obtained on frequency response. Then, since the substrate amplitude level overlaps the tag amplitude signal, a dip in frequency response can be noticed. (IV) the resonant to quasi-optic amplitude level has 5 dB, which means that the frequency response presents a peak with an amplitude equivalent to the difference between the signal's amplitude.

The *a priori* knowledge of the environment is imperative to chipless system implementation. Indeed, when the tag is placed on different objects, the backscattered diagram changes. Then, it allows retrieving the tag ID in preferred angular

regions, as depicted in Fig. 8. Indeed, object geometry changes modify the RQMR level. A single input multiple output system may be employed in this practical situation, where multiple antennas can focalize on different angles. For instance, in Fig. 8, we must use an antenna array to retrieve the maximum RQMR. Considering the object dimension $D_{obj} = 200$ mm, we must place the antenna at $\beta = 56°$. In this situation, the quasi-optic mode level can be neglected compared to the measurement when the tag is present. Considering the dimension $D_{obj} = 250$ mm, an additional antenna can be used at $\beta = 42°$ to recover the signal and maximize the RQMR. Then, for more robust system implementation, an antenna array must be employed.

In order to emphasize the encoding information possibility from this presented approach, a tag composed of 7-resonant dipoles is developed considering the previous ground plane. Hence, the 7-resonant elements have different lengths, thus, different resonance frequencies. As we can see in Fig. 9, the prominent peaks at $\beta = 56°$ indicate a high RQMR. However, when $\beta = 0°$, the low level of each frequency denotes a low RQMR. It is noteworthy that even when $\beta = 56°$, the last resonance is negatively impacted. Then, its RQMR is reduced due to the interaction with the ground plane. Therefore, another ground plane dimension can be used to increase the number of resonances.

IV. Experimental Setup and Measurements

The measurements were performed with an Agilent N5222A $(0.01\ \text{GHz} - 26.5\ \text{GHz})$ PNA. A circular probe array system (StarLab form MVG) is used to measure the radiation pattern, such as a multi-probe spherical system. As shown in Fig. 10(a), the entire setup is surrounded by absorbing materials, which reproduce the free space condition. The spherical systems are composed of two arrays of probes installed on an arch of 45 cm radius. The probe array allows electronic scanning. The probes array is intended for measurements on a $0.65\ \text{GHz} - 6.0\ \text{GHz}$ frequency range. The probes consist of two orthogonal arrays on the circular structure, each probe has two antennas linearly polarized and aligned according to horizontal and vertical polarization, (R_ϕ, R_θ), respectively

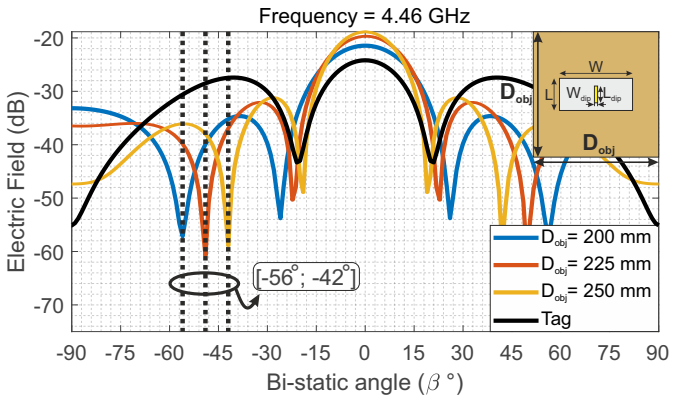

Fig. 8: Diagram pattern of the tag response for different dimensions of the object on which the tag is positioned. Different maximum RQRM are noticed with the geometrical variations.

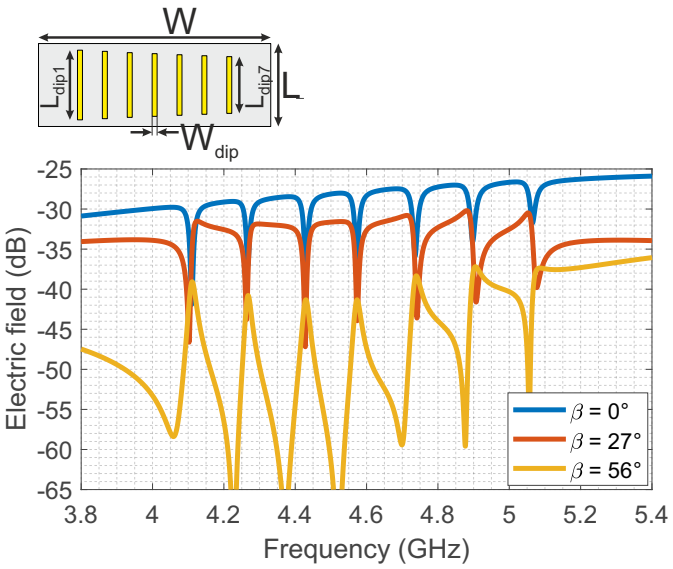

Fig. 9: E-field co-polarized frequency response from a 7-resonator tag at two different angles β.

[see inset in Fig. 10(a)]. A mechanical arch movement allows performing measurements along ϕ-rotation. The probes array rotates with a step of $\Delta\beta = 0.5°$ according to the ϕ-angle so that the probes are positioned in offset locations. Here only the probe number 3 was used, the measurements are done on $\beta \in [48.75°,\ 63.75°]$ angular range, as seen in Fig. 10(b), whereas the probe-3 covers the optimum angle in our case.

The transmission antenna (QH800) from MVG) is linearly polarized (R_θ) and operates in the $0.8\ \text{GHz} - 12\ \text{GHz}$ range with a gain of $5\ \text{dBi} - 10\ \text{dBi}$. The tag is positioned at the arch center, as seen in Fig. 10. The support on which the tag is placed is microwave transparent in the considered bandwidth. Consequently, the tag is measured in three different configurations: first, without the presence of objects and any post-processing. Then, the tag is placed on an object, and the measurements are made. Finally, the time-gating filtering is considered with the object's presence.

V. Anechoic Environment Measurements

Three antenna measurement configurations are evaluated for comparison purposes in an anechoic chamber (StarLab form MVG):

- S_{11}: Mono-static measurement. The transmit antenna (QH800 from MVG), receives the signal.
- $S_{21}(\beta = 2.5°)$: the bistatic configuration at $\beta \approx 0°$, where the isolation between the antennas is greater than 20 dB. One antenna is the (QH800) and the other is the probe number 1.
- $S_{21}(\beta = 60°)$: the bistatic configuration at $\beta \approx 56°$. In this case the QH800 antenna and the probe number 3 are used.

A classical calibration method has been used to extract the resonance frequencies of the tag $(f_1, \cdots, f_7)$. This way, the knowledge of the exact resonance frequencies is assured for the rest of the study. Vertical dashed lines in the figures

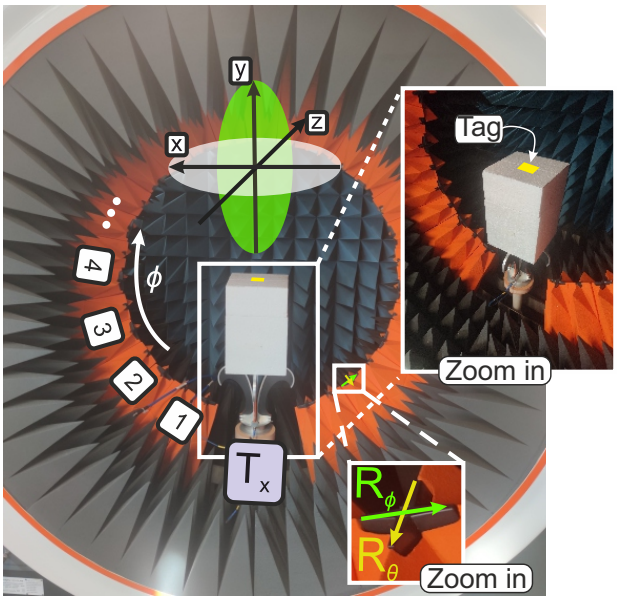

(a)

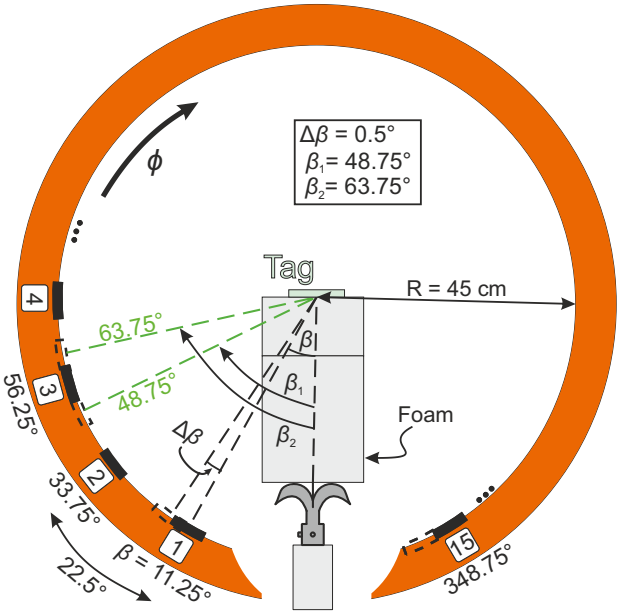

(b)

Fig. 10: (a) The electronic and mechanical scanning spherical measurement setup, (b) geometrical configuration of spherical setup.

indicate these frequencies presented backscattering field measurements. It is useful for comparison purposes.

The tag based on multiple half-dipoles that can operate from 4.25 GHz to 5.5 GHz and introduced in Section II has been fabricated (see Fig. 11). The proposed technique is evaluated through the measurements of this tag. Furthermore, the simplicity of the tag used allows a straightforward assessment of the technique.

A. Evaluation on raw measurements

Measurements are evaluated without any post-processing. Considering the mono-static $|S_{11}|$ measurements, as shown in Fig. 12, the frequency response does not present any marked

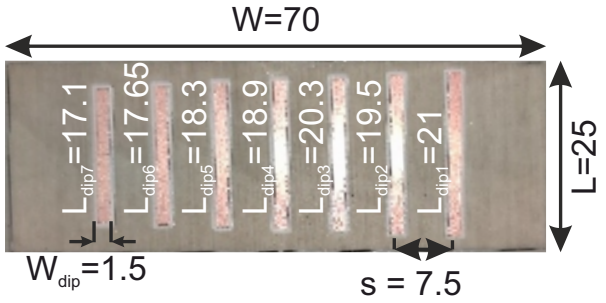

Fig. 11: Fabricated 7-resonator tag backed by a ground plane, all dimensions are in millimeter.

resonances. Hence, the low RQMR (due to a high quasi-optic mode amplitude level present in the tag response) provides a signal in which the tag information is not readable. In bistatic configuration $|S_{21}(\beta = 2.5°)|$, a high reflection is highlighted mainly due to the ground plane reflection, but some low-level dip resonances are seen in Fig. 12, which indicates that the bistatic configuration improves the RQMR. Then, the $|S_{21}(\beta = 60°)|$ is evaluated; it is possible to identify prominent peaks and dips, which were not notable considering the previous measurements ($|S_{11}|$ and $|S_{21}(\beta = 2.5°)|$). Note that even without any post-processing, the tag encoded information can be retrieved, indeed with the $|S_{21}(\beta = 60°)|$ measurement, the tag frequency response shows dips/peaks. Since the tag is analyzed at different frequencies, the whole backscattered diagram changes mainly due to the ground plane influence. Then, for some frequencies, the RQMR is maximum. However, for some of them, mainly (f_7), the RQMR is negatively impacted, and the $Q-$factor, the same situation is highlighted previously in Fig. 9.

B. Assessment of raw measurements in object presence

As depicted in Fig. 13, a magazine is used as an object on which the tag is placed. The presence of the object significantly increases the quasi-optic mode, and a flat frequency

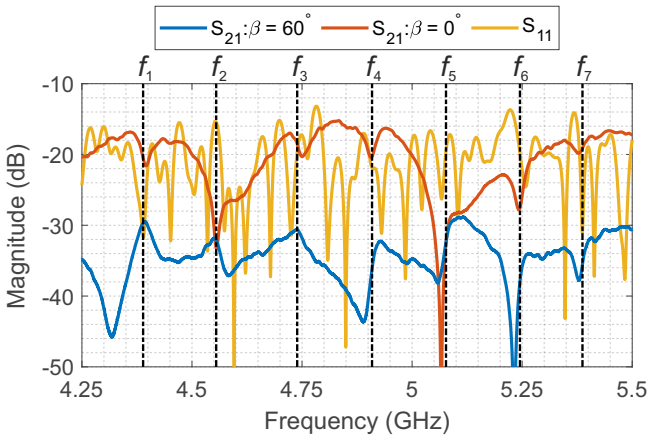

Fig. 12: Frequency domain response raw measurements for mono-static configuration $|S_{11}|$ and bistatic configurations $|S_{21}(\beta = 2.5°)|$ and $|S_{21}(\beta = 60°)|$. The resonant frequencies $(f_1, \cdots, f_7)$ have been characterized in anechoic chamber using a calibration technique.

response can be observed in Fig. 14, in the case of the mono-static $|S_{11}|$ and bistatic $|S_{21}(\beta = 2.5°)|$ configuration. On the $|S_{21}(\beta = 60°)|$ measurement, peaks and dips are evident. However, due to the high level of the quasi-optic mode, for several frequencies (excepted f_1 and f_2), the response presents shifted peaks or dips. Therefore, the time-gating technique must be performed to access the exact resonance frequencies.

Note that to improve the results in case of the object's presence, the curves presented in Fig. 14 are obtained by subtracting the measurements of the tag from the empty measurement (S_e). The empty measurement is done without the object and the tag's presence. Notably, this post-processing operation is independent of the scenario and can still be used in practical applications. Furthermore, this previous subtraction allows removing the effect of the antenna mismatch.

C. Evaluation of measurements on object presence with time-gating filtering

As clearly seen in Figs. 12 and 14, some peaks and dips are shifted from the expected resonance frequencies (as described theoretically in [19]), which can significantly affect the robustness of the reading. Consequently, a signal post-processing step is required to correct the reading process. A common way to remove partially the clutter contributions from the tag response is to filter the incoming signals on the time-domain as shown in Fig. 15 [18], [13]. For this purpose, a time-window is positioned after the main first object reflection (t_{start}) until the last resonant time (t_{stop}), thus removing the quasi-optic mode at the beginning of the signal [13]. After the time domain filtering, the time signal is converted into the frequency domain. It is important to point out that all signals processed to use the same rectangular window length (the first strong quasi-optic contribution is removed from the signals). Furthermore, the empty subtraction has been performed before the time-gating operation.

The magnitude of the frequency domain signals after time-domain filtering is depicted in Fig. 16. Indeed, the $|S_{21}(\beta = 60°)|$ presents precise resonance frequencies denoted by the peak apex even in the presence of the object. This is not the case for $|S_{21}(\beta = 2.5°)|$ and $|S_{11}|$, that undergo a high-level quasi-optic influence in the response, as depicted in Fig. 16.

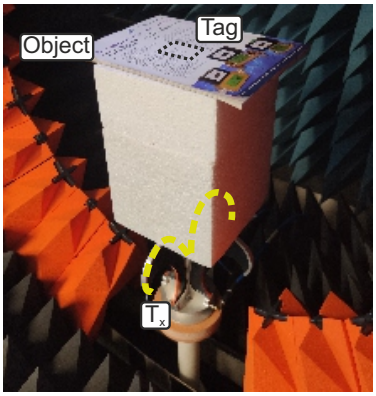

Fig. 13: Anechoic environment considering the tag and an object.

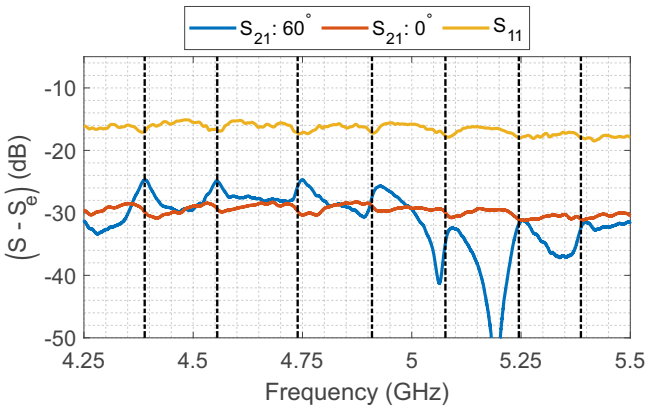

Fig. 14: Subtraction of the raw measurements from the empty measurement for mono-static configuration $|S_{11}|$ and bistatic configurations $(|S_{21}(\beta = 2.5°)|; |S_{21}(\beta = 60°)|)$ considering an object.

VI. Real environment measurements

In order to assess the effectiveness of the proposed approach, the 7-resonator tag introduced in section II.C has been measured in a real environment. The response of the tag has been measured using two vertical-polarized horn antennas (QH2000) in bistatic configuration at an angle $\beta = 60°$ on a 4.25 GHz $-$ 5.5 GHz frequency range with a gain of 5 dBi $-$ 9 dBi. The tag was placed at a distance of 15 cm from the antennas; the setup is depicted in Fig. 17. To assess the robustness of the presented method, the tag has been measured when attached to different objects: a book, a metal plate, a carton box, and a plastic box. The metal plate case with dimensions 350 mm $\times$ 800 mm, can be seen in Fig. 17. It is noted that the objects used are different from each other both in terms of materials and dimensions. Indeed, none of these materials have the same dimensions as those simulated in section II.C (see Fig. 8). The objective here is to show the robustness of the approach whatever the objects on which the tags will be positioned.

The frequency magnitude signals $|S_{21}(\beta = 60°)|$ without any post-processing are depicted in Fig. 18. The measurement results of the four different objects have similar behavior,

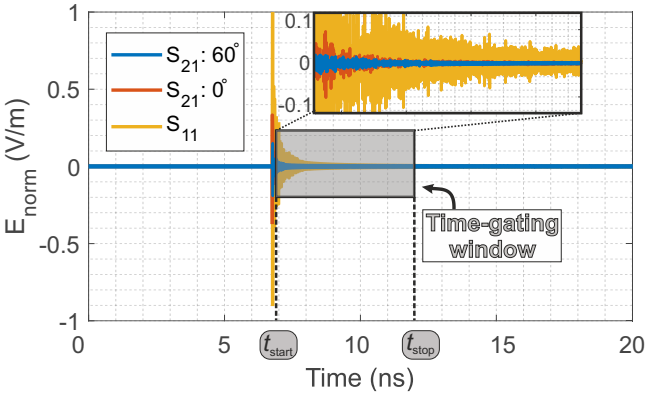

Fig. 15: Temporal domain filtered signals in mono-static and bistatic configurations considering the presence of an object. The time start $(t_{start} = 6.82$ ns) and time stop $t_{stop} = 12$ ns of the time-gating window for the analyzed signals.

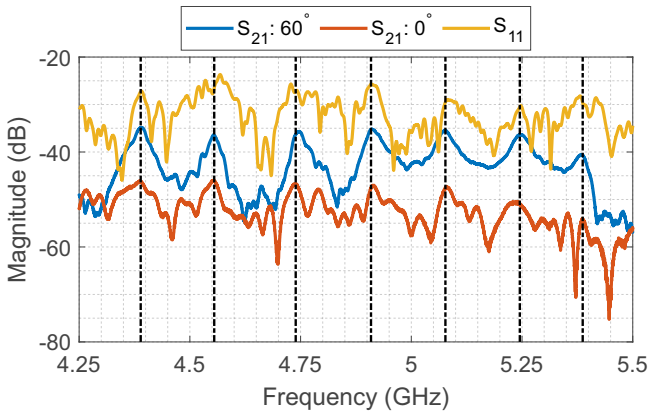

Fig. 16: Frequency domain signal considering time-domain filtering in mono-static and bistatic configurations in the presence of an object.

indicating that the signals do not depend on which object the tag is placed on. Since most of the quasi-optic mode is reduced by bistatic diversity, the tag response exhibits approximately the same characteristics. However, the quasi-optic mode directly impacts the frequency peak positions. Therefore, a simple time-gating filtering step is necessary to extract the resonance frequencies by removing the rest of the quasi-optic mode.

The time window starts immediately after the first strong peak in the temporal signal representation; meanwhile, the window is long enough to get the late-time response. After the time filtering, the frequency responses are depicted in Fig. 19. The frequency response for all the objects presents the same peak apex position, which perfectly matches the expected resonance frequencies.

Note that in addition to the spatial diversity, temporal filtering must be employed to extract the resonance frequencies of the tag. It must point out that these results are not achievable with the classic approach, *i.e.*, $|S_{21}(\beta \approx 0°)|$ and time gating. Nevertheless, the proposed technique paves the way for new chipless RFID system implementations. Besides, new RFID chipless systems can implement this technique to increase the

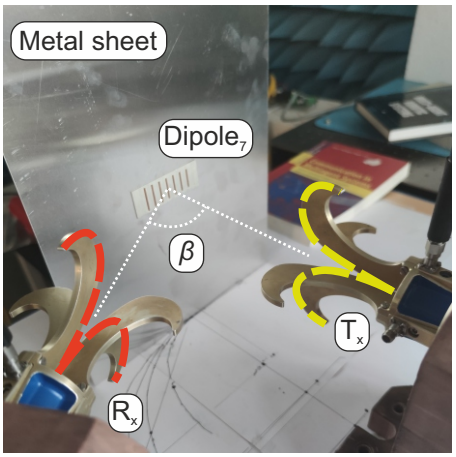

Fig. 17: Real environment setup, the antennas are co-polarized following a β-angle.

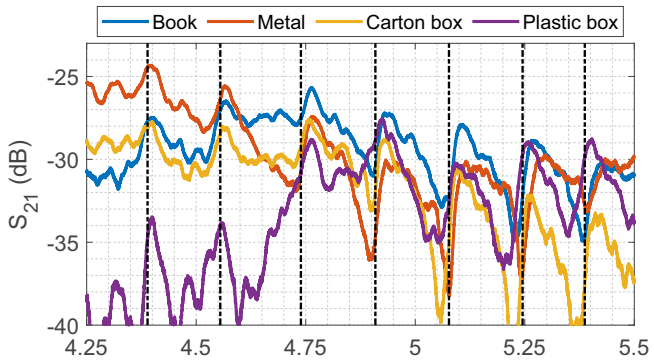

Fig. 18: $|S_{21}(\beta = 60°)|$ raw measurements in frequency domain considering different objects and in real environment.

system's robustness as a whole, where several antennas can be used in specific locations (different β-angle), thus increasing the reading reliability.

VII. Tag performance under real reading situations

In this study, real non-systematic errors that can impact the tag response are assessed to ensure the robustness of detection for real-environment applications. For these measurements, the time-gating filtering is done.

Using a bistatic reading configuration imposes positioning the tag in a specific area of the space and with a given angle (normal incidence). So it is interesting to evaluate possible errors in the position or orientation of the tag. Indeed, the tag's translation or rotation can be considered in system implementation. As the measurements have been performed at a fixed β-angle with a reading range of 15 cm, the translation error (δ) means that the tag is shifted according to the linear polarized transmission wave, as shown in Fig. 20. The rotation represents the angular rotation around the support axis itself as depicted in Fig. 20; the angle (α) can assume positive and negative values. The positive values indicate that the tag turns toward the reception antenna. In contrast, the negative angular values $(-\alpha)$ indicate that the tag rotates in the opposite direction of the receiving antenna. The time-gating is applied to the time domain signal. Finally, a reading range study is

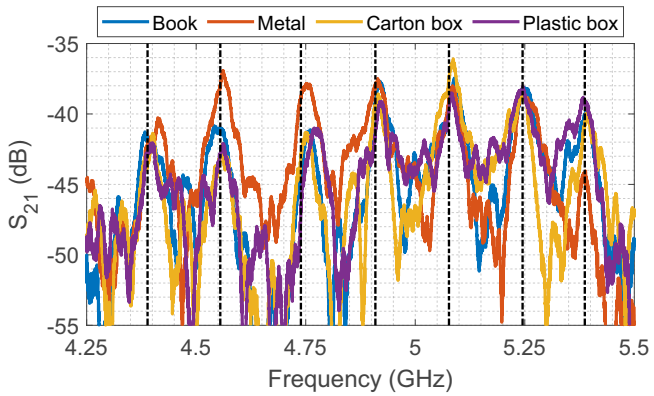

Fig. 19: $|S_{21}(\beta = 60°)|$ co-polarized time-windowed signals in frequency domain considering different objects.

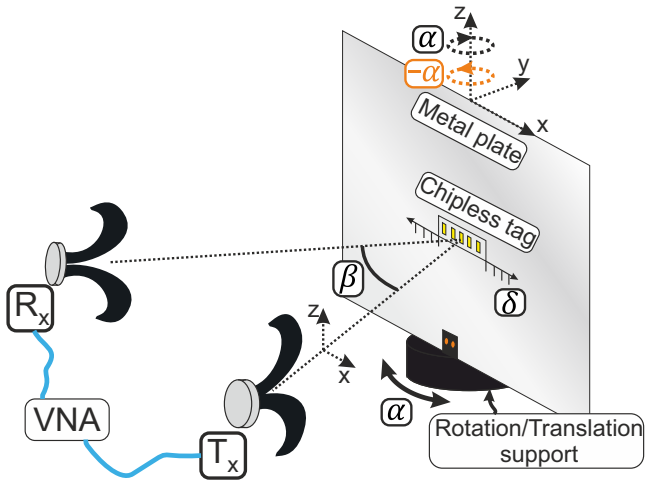

Fig. 20: Support for tag rotation/translation error study. The rotation is around the support axis itself, whereas the translation is by changing the positions following the x-axis.

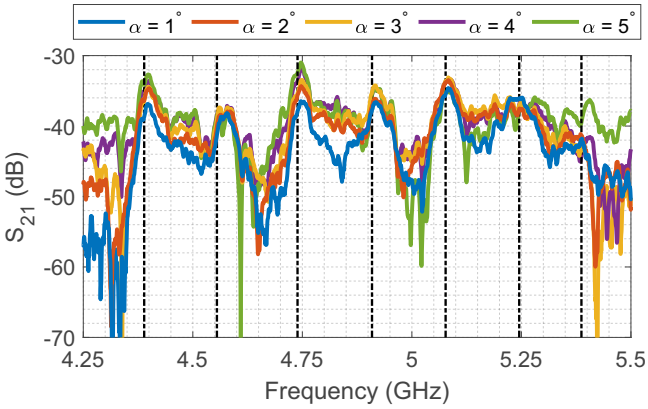

Fig. 21: Misalignment study with a metal plate: $|S_{21}(\beta = 60°)|$ measurements for different positives α-angles.

evaluated for a constant β-angle. Henceforth, the criterion to define tag detection consists of retrieving all tag resonances at the expected frequencies.

A. Non-systematic errors evaluation

In real reading situations, non-systematic errors are naturally introduced by non-desired misalignments. For instance, misalignments when the tag is placed on an object or antenna's angular misalignment due to tag rotation. Therefore, studying these errors is essential to assess the proposed technique completely.

The $|S_{21}(\beta = 60°)|$ frequency response to positive rotation (α) is shown in Fig. 21. In this configuration, the quasi-optic mode is higher due to tag and metal plate rotation toward the R_x antenna. Then, following the criterion previously established, the tag can be read up to an angle α of 3°. It is noteworthy that even when all resonances cannot be retrieved, the backscattered signals provide consistent resonances for each signal's first, third, and fourth resonances.

The frequency response with negative rotation $(-\alpha)$ is depicted in Fig. 22. Considering the angular positions, a part of the quasi-optic mode is directed far from the R_x antenna. Therefore, the signals are less impacted by the quasi-optic mode characterized by a well-marked peak apex on the frequency response. The angle range to completely retrieve the tag information in such a case is $0° \leq \alpha \leq 7°$.

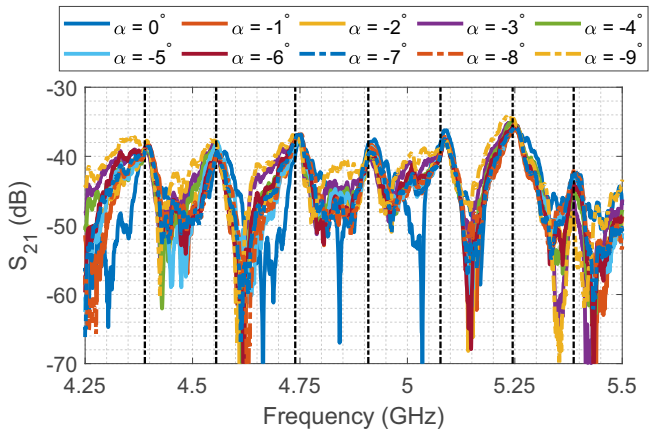

Fig. 22: Misalignment study with a metal plate: frequency response $|S_{21}(\beta = 60°)|$ measurements for different negative α-angles.

The β-angle between the antennas is still fixed, and now the S_{21} measurements are performed, shifting the tag position following the x-axis. Steps of $\delta = 5$ mm have been considered, the magnitude of S_{21} is shown in Fig. 23. Whole resonances can be recovered until a displacement of 15 mm, which means that considering an application, the tag can have a misalignment of -15 mm $< \delta <$ 15 mm between the R_x and T_x antenna.

B. Reading range

Finally, the reading range is evaluated by our proposed technique. All signals are temporally aligned; thus the time-windowing is applied, while the T_x and R_x antennas are displaced, maintaining the β-angle between the antennas, as shown in Fig. 24.

The S_{21} measurements for each distance are shown in Fig. 25. Up to 15 cm, all resonances can be measured; after that, reading all resonances becomes difficult due to a lower SNR. A significant reduction in the distance related to the real environment condition is noted. In fact, in the anechoic

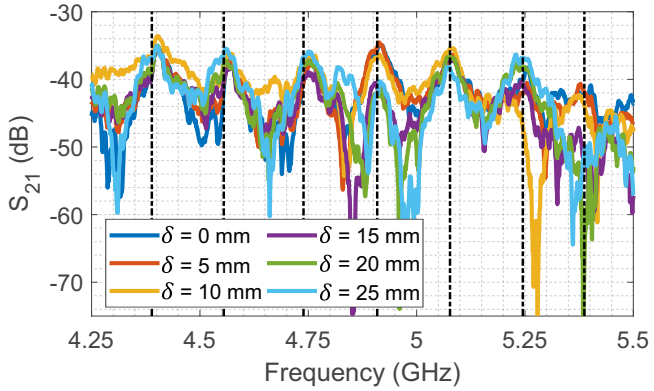

Fig. 23: Misalignment study with a metal plate: $|S_{21}(\beta = 60°)|$ measurements for different δ values.

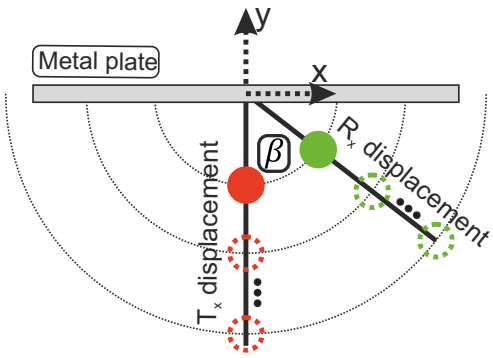

Fig. 24: Reading range configuration study: $|S_{21}(\beta = 60°)|$ measurements for different distances between the tag and the antennas maintaining the bistatic configuration with $\beta = 60°$.

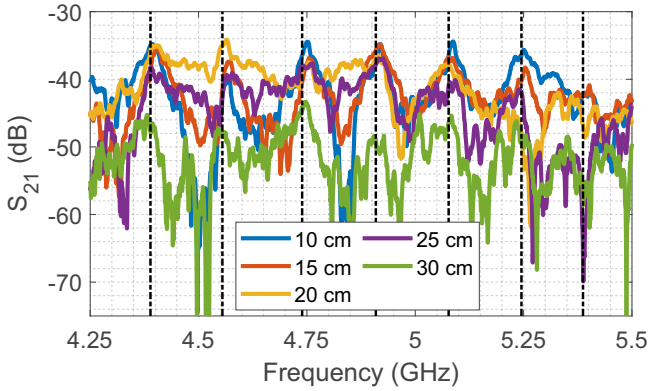

Fig. 25: Reading range study with a metal plate: $|S_{21}(\beta = 60°)|$ measurements with time gating considering the distances between the tag and the antennas maintaining the bistatic configuration with $\beta = 60°$.

environment used in Section III, the reading distance was around 45 cm (see Fig. 10).

The technique presented in this article proposes a single measurement to retrieve the chipless tag ID with a simple additional post-processing step. Additionally, high reflective environments are evaluated in different conditions. These results show that the proposed technique must fulfill the following conditions:

- The maximum tag rotation (α) considering the two antennas configuration (T_x and R_x with a β-angle) is $-7° \leq \alpha \leq 3°$.
- The translation (δ) must be less than 3 cm $(-1.5 \text{ cm} < \delta < 1.5 \text{ cm})$.
- A reading ranges up to 15 cm.

Note that this is the result for the configuration with two antennas only. However, a larger reading volume can be obtained by using more than two antennas. In this case, the improvement of the RQMR can be obtained over a larger frequency band which will significantly improve the robustness of the reading and the reading area.

Therefore, the radiation pattern of the chipless tags is quasi-omnidirectional considering half- and quarter-wave scatterer resonators. For tags with a ground plane, the dimension of the ground plane significantly impacts the total re-radiation pattern. Further, the angle between the two antennas can be optimized to a first approximation based on the ground plane size. Then, when 60° angle is not optimal, it already filters most of the clutter contributions (as shown in Section III). This is also true for different types of environments, an angle of 60° for reading distances of a few tens of centimeters will allow reducing a significant part of the clutter contributions. Additionally, the shape of these scatterers or their number will not modify this re-radiation pattern significantly since resonant elements are considered.

VIII. Tag Decoding Scheme

Two distinct situations are analyzed to address the issue of the evaluation of post-processing techniques in chipless applications. The measurement was done either in two different environments. Then, the post-processing step is performed on the raw signals. Firstly, the measurements were carried out in an open environment and performed on a large metallic table. Thus, in this particular case, [namely environment-1 (E_1)], the environment does not present any object near the tag; there are simply reflections on the walls and ceiling several meters behind the tag. In the second environment, the setup is placed in a semi-anechoic chamber where some objects are introduced in the tag vicinity, namely environment-2 (E_2). The object's vicinity increases the level of the quasi-optic reflections. Then, to assess the tag robustness, the 7-dipoles tag backscattered signal is recorded considering the S_{11} and $S_{21}(\beta = 60°)$. It is noteworthy that no empty calibration is applied to the signals, and the same time-gating has been applied.

Note that the environment E_1 not presenting any object near the tag is thus not an environment particularly favorable to the method (the power of the signal backscattered in bistatic for an angle of $\beta = 60°$ is necessarily weaker than that obtained in mono-static). Contrarily, the environment E_2, presenting objects close to the tag, is typically a good example of environments for which the method was introduced.

As depicted in Fig. 26, the frequency- and time-domain curves have been plotted. The curves show the behavior for to different configurations: $|S_{11}|$ and $|S_{21}|$. Note that for both environments, the $S_{21}(\beta = 60°)$ presents a lower signal level at low and high frequencies. Since the same time-gating is applied, for $S_{21}(\beta = 60°)$, this low environment level is achieved with the bistatic measurement diversity.

In Fig. 27(a), for E_2, the $S_{21}(\beta = 60°)$ shows well marked peaks, meanwhile the S_{11} backscattered signal is negatively impacted by these quasi-optic reflections (even with time-gating).

As depicted in Fig. 26(b), without any object in the tag vicinity, reflections from far-distance targets fall in late-time response, which directly impacts the RQMR by the less marked peaks. On the other hand, when objects are placed in the tag vicinity, as shown in Fig. 27(b), two contributions appear in the early time: in addition to a first reflection which arises from the antenna to the cable connection, meanwhile, a second main reflection relies upon the tag and objects quasi-optic reflections. Further, the S_{21} measurement retains the first and second peak in the early time. The reflection seen in early time is due to the antenna reflection. It is important to note

TABLE I: Results of the automatic decoding algorithm in the case of environment-1. Number 1 corresponds to the first peak position and the 7 the last. DPA threshold of 0.04 has been attributed.

Environment 1 (E_1)		**1**	**2**	**3**	**4**	**5**	**6**	**7**
S_{11}	sub-bands	"1"	"1"	"1"	"1"	"1"	"1"	"0"
	DPA	0.131 "1"	0.102 "1"	0.221 "1"	0.187 "1"	0.242 "1"	0.001 "0"	0.121 "1"
	Combined results	"1"	"1"	"1"	"1"	"1"	"0"	"0"
S_{21}	sub-bands	"1"	"1"	"1"	"1"	"1"	"1"	"1"
	DPA	0.191 "1"	0.223 "1"	0.265 "1"	0.131 "1"	0.151 "1"	0.193 "1"	0.019 "1"
	Combined results	"1"	"1"	"1"	"1"	"1"	"1"	"1"

TABLE II: Results of the automatic decoding algorithm in the case of environment-2. Number 1 corresponds to the first peak position and the 7 the last. DPA threshold of 0.04 has been attributed.

Environment 2 (E_2)		**1**	**2**	**3**	**4**	**5**	**6**	**7**
S_{11}	sub-bands	"1"	"1"	"1"	"1"	"1"	"1"	"1"
	DPA	0.132 "1"	0.123 "0"	0.164 "1"	0.097 "1"	0.042 "1"	0.007 "0"	0.046 "1"
	Combined results	"1"	"0"	"1"	"1"	"1"	"0"	"1"
S_{21}	sub-bands	"1"	"1"	"1"	"1"	"1"	"1"	"1"
	DPA	0.086 "1"	0.148 "1"	0.126 "1"	0.143 "1"	0.151 "1"	0.169 "1"	0.079 "1"
	Combined results	"1"	"1"	"1"	"1"	"1"	"1"	"1"

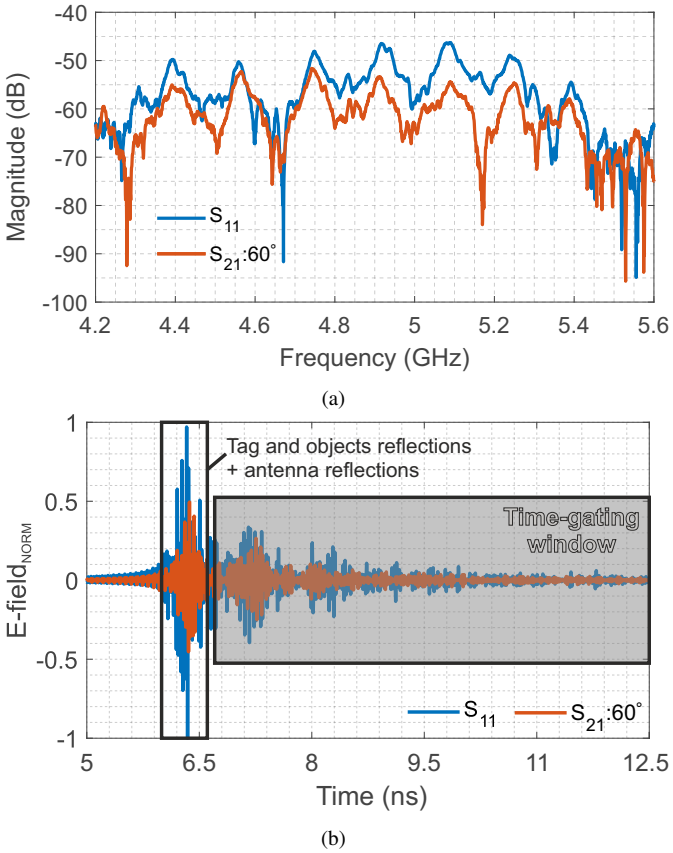

Fig. 26: (a) the frequency response for the environment without objects in tag vicinity (E_1), (b) time-domain response. The signals were normalized considering the higher magnitude among the two signals.

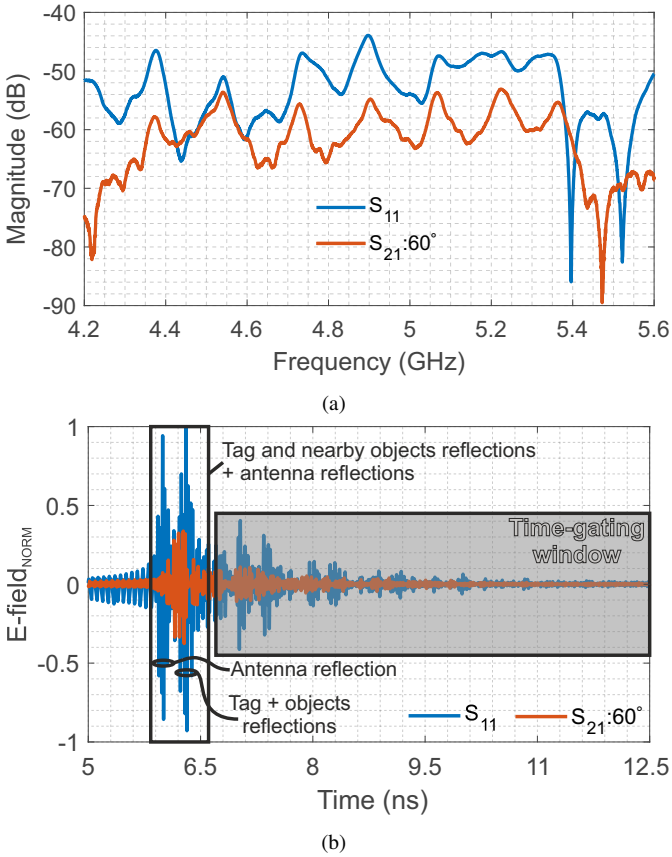

Fig. 27: The frequency response for objects in tag vicinity (semi-anechoic chamber E_2). The objects placed in the environment are unchanged for S_{11} and S_{21} configurations. The signals were normalized considering the higher magnitude among the two signals.

that the quasi-optic mode from near contributions is highly decreased by the bistatic measurement (S_{21}).

In order to analyze the reliability and robustness of the proposed approach, an automatic decode algorithm has been implemented. Firstly, the measured signal is correlated to a gaussian signal. The normalized cross-correlation is a simple and efficient way to suppress the presence of peaks unrelated to a resonance frequency. The result of the correlation can be used directly to identify the resonance frequencies through the calculation of the maximums of the curve. The approach to identifying the tag is as follows: the cross-correlation is first obtained. Then all the peaks on that signal are computed, and only the seven peaks with the highest correlation values are selected. We evaluate afterward in which sub-band they belong, as we can see in Fig. 28. As long as we know the ID of the measured tag, we can compare the sub-bands where a peak is present with the expected result to verify the result. If a peak belongs to an expected sub-band, the value "1" is attributed, and "0" otherwise. Moreover, a metric based on the dip-to-peak amplitude (DPA) has been performed (see Fig. 28). The DPA quantifies the level difference between the peak and the left first valley. Fig. 28 show the cross-correlation result

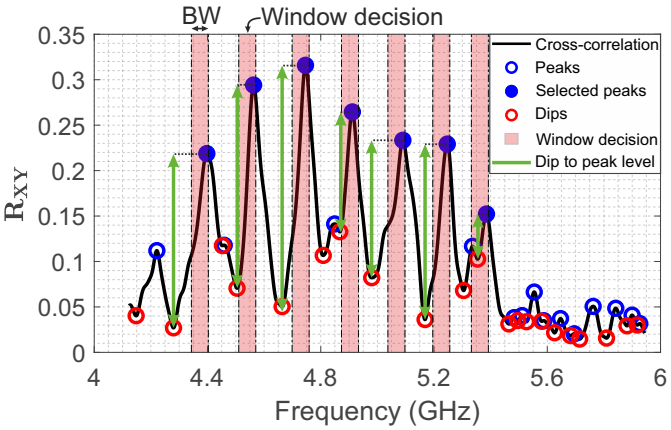

Fig. 28: Cross-correlation result obtained for the S_{21} signal as a function of the frequency for the environment-1 (E_1). The bandwidth of 40 MHz around the resonance peak was considered for the decoding algorithm.

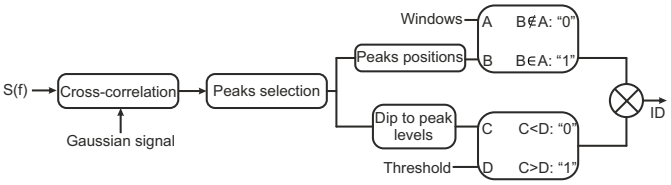

Fig. 29: Decoding steps for tag identification

and the metrics involved in the decoding algorithm.

In order to protect against false detection (typically peaks apex with amplitudes too close to the noise level), a threshold is established. For each of the seven peaks, a DPA value higher than a threshold relating to the "1" and "0" otherwise. It should be noted that the metric can be used to increase the robustness of decoding. Therefore, the DPA highlights the resonant level compared to the clutter contributions.

Finally, if the peak is placed inside the correct sub-band and the DPA is superior to the threshold, we get "1" for an expected correct detection. However, if one of these conditions is false, the "0" value is attributed. The block diagram of the decoding algorithm is presented in Fig. 29. The obtained ID's are resumed in the Table I and Table II. The metrics are used in both environments and reading configurations. In the environment E_2 for $S_{21}(\beta = 60°)$, the ID of the 7-dipole tag is successfully detected. However, the S_{11} presents some misclassifications, precisely regarding the higher frequency resonances. These resonances are highly due to clutter contributions. For environment E_1, the $S_{21}(\beta = 60°)$ allows correct decoding, meanwhile the S_{11} is more impacted.

IX. Conclusions

A bistatic diversity method for chipless tag identification purposes has been introduced and evaluated. A simple dipole resonator was first modeled analytically and hereafter simulated to assess the approach. The scattered electric field of chipless tags has been analytically calculated relying on general scatter theory. The separation between the scatters mechanisms that compose the total scattered field was calculated. The resonant and structural modes were approximated to two independent contributions. Then, the modeling assessed the feasibility of the approach, and, finally, a 7-resonator dipoles tag was measured in an anechoic and a real-scenario environment. The backscattered pattern is established at the resonance frequency considering the co-polarization of the analyzed tag as a function of the angle between the transmission and reception antennas (β). When an object is considered in the measurements, one simple additional post-processing method is cooperatively used. Therefore, the peak's apex is retrieved and confirmed by comparison with the expected tag's resonance frequencies. This is obtained even though the highly reflective characteristic of the objects used in a real environment. Real-environment limitations considering the worst scenario were evaluated. This technique can significantly increase the robustness of the chipless tag system, thus increasing the reading reliability without a calibration measurement.

Acknowledgement

The authors would like to acknowledge the University Grenoble Alpes for financially supporting this project AUSTRALE via the ANR program. This project has also received funding from the European Research Council (ERC) under the European Union's Horizon 2020 Research and Innovation Program (ScattererID - grant agreement N° 772539).

References

[1] E. Perret, *Radio Frequency Identification and Sensors: From RFID to Chipless RFID*. John Wiley & Sons, Dec. 2014.

[2] A. Chamarti and K. Varahramyan, "Transmission Delay Line Based ID Generation Circuit for RFID Applications," *IEEE Microwave and Wireless Components Letters*, vol. 16, no. 11, pp. 588–590, Nov. 2006.

[3] C. M. Nijas, R. Dinesh, U. Deepak, A. Rasheed, S. Mridula, K. Vasudevan, and P. Mohanan, "Chipless RFID Tag Using Multiple Microstrip Open Stub Resonators," *IEEE Transactions on Antennas and Propagation*, vol. 60, no. 9, pp. 4429–4432, Sep. 2012.

[4] R. S. Nair and E. Perret, "Folded Multilayer C-Sections With Large Group Delay Swing for Passive Chipless RFID Applications," *IEEE Transactions on Microwave Theory and Techniques*, vol. 64, no. 12, pp. 4298–4311, Dec. 2016.

[5] I. Jalaly and I. Robertson, "Capacitively-tuned split microstrip resonators for RFID barcodes," in *2005 European Microwave Conference*, vol. 2, Oct. 2005, pp. 4 pp.–1164.

[6] A. Vena, E. Perret, and S. Tedjini, "Chipless RFID Tag Using Hybrid Coding Technique," *IEEE Transactions on Microwave Theory and Techniques*, vol. 59, no. 12, pp. 3356–3364, Dec. 2011.

[7] ——, "RFID chipless tag based on multiple phase shifters," in *2011 IEEE MTT-S International Microwave Symposium*, Jun. 2011, pp. 1–4.

[8] D. Girbau, A. Ramos, A. Lazaro, S. Rima, and R. Villarino, "Passive Wireless Temperature Sensor Based on Time-Coded UWB Chipless RFID Tags," *IEEE Transactions on Microwave Theory and Techniques*, vol. 60, no. 11, pp. 3623–3632, Nov. 2012.

[9] A. Vena, E. Perret, and S. Tedjni, "A Depolarizing Chipless RFID Tag for Robust Detection and Its FCC Compliant UWB Reading System," *IEEE Transactions on Microwave Theory and Techniques*, vol. 61, no. 8, pp. 2982–2994, Aug. 2013.

[10] F. Costa, S. Genovesi, and A. Monorchio, "Normalization-Free Chipless RFIDs by Using Dual-Polarized Interrogation," *IEEE Transactions on Microwave Theory and Techniques*, vol. 64, no. 1, pp. 310–318, Jan. 2016.

[11] S. Genovesi, F. Costa, F. A. Dicandia, M. Borgese, and G. Manara, "Orientation-Insensitive and Normalization-Free Reading Chipless RFID System Based on Circular Polarization Interrogation," *IEEE Transactions on Antennas and Propagation*, vol. 68, no. 3, pp. 2370–2378, Mar. 2020.

[12] R. Rezaiesarlak and M. Manteghi, "Short-Time Matrix Pencil Method for Chipless RFID Detection Applications," *IEEE Transactions on Antennas and Propagation*, vol. 61, no. 5, pp. 2801–2806, May 2013.

[13] A. Ramos, E. Perret, O. Rance, S. Tedjini, A. Lazaro, and D. Girbau, "Temporal Separation Detection for Chipless Depolarizing Frequency-Coded RFID," *IEEE Transactions on Microwave Theory and Techniques*, vol. 64, no. 7, pp. 2326–2337, Jul. 2016.

[14] J. A. Vitaz, A. M. Buerkle, M. Sallin, and K. Sarabandi, "Enhanced Detection of On-Metal Retro-Reflective Tags in Cluttered Environments Using a Polarimetric Technique," *IEEE Transactions on Antennas and Propagation*, vol. 60, no. 8, pp. 3727–3735, Aug. 2012.

[15] J. G. D. Hester and M. M. Tentzeris, "Inkjet-Printed Flexible mm-Wave Van-Atta Reflectarrays: A Solution for Ultralong-Range Dense Multitag and Multisensing Chipless RFID Implementations for IoT Smart Skins," *IEEE Transactions on Microwave Theory and Techniques*, vol. 64, no. 12, pp. 4763–4773, Dec. 2016.

[16] S. Preradovic, I. Balbin, N. C. Karmakar, and G. F. Swiegers, "Multiresonator-Based Chipless RFID System for Low-Cost Item Tracking," *IEEE Transactions on Microwave Theory and Techniques*, vol. 57, no. 5, pp. 1411–1419, May 2009.

[17] D. Girbau, J. Lorenzo, A. Lazaro, C. Ferrater, and R. Villarino, "Frequency-Coded Chipless RFID Tag Based on Dual-Band Resonators," *IEEE Antennas and Wireless Propagation Letters*, vol. 11, pp. 126–128, 2012.

[18] D. Girbau, A. Lazaro, and A. Ramos, "Time-coded chipless RFID tags: Design, characterization and application," in *2012 IEEE International Conference on RFID-Technologies and Applications (RFID-TA)*, Nov. 2012, pp. 12–17.

[19] Z. Ali, E. Perret, N. Barbot, and R. Siragusa, "Extraction of Aspect-Independent Parameters Using Spectrogram Method for Chipless Frequency-Coded RFID," *IEEE Sensors Journal*, vol. 21, no. 5, pp. 6530–6542, Mar. 2021.

[20] S. Kofman, Y. Meerfeld, M. Sandler, S. Dukler, and V. Alchanatis, "Radio Frequency Identification System and Data Reading Method," US Patent US 8,167,212, Sep., 2007. [Online]. Available: https://patentscope.wipo.int/search/en/detail.jsf?docId=WO2007102142

[21] M. Zomorrodi and N. C. Karmakar, "Optimized MIMO-SAR Technique for Fast EM-Imaging of Chipless RFID System," *IEEE Transactions on Microwave Theory and Techniques*, vol. 65, no. 2, pp. 661–669, Feb. 2017.

[22] M. Pöpperl, J. Adametz, and M. Vossiek, "Polarimetric Radar Barcode: A Novel Chipless RFID Concept With High Data Capacity and Ultimate Tag Robustness," *IEEE Transactions on Microwave Theory and Techniques*, vol. 64, no. 11, pp. 3686–3694, Nov. 2016.

[23] R. Hansen, "Relationships between antennas as scatterers and as radiators," *Proceedings of the IEEE*, vol. 77, no. 5, pp. 659–662, May 1989.

[24] C. A. Balanis, *Antenna theory: analysis and design*. John wiley & sons, 2015.

Raymundo de Amorim Junior received the B.S. degree in electrical engineering and M.S. degree in telecommunications and electronics, both from Universidade Federal de Campina Grande, Campina Grande, Brazil, in 2016 and 2018, respectively. From 2013 to 2018, he was a member Applied Electromagnetics and Microwave Laboratory (LEMA). He is currently pursuing the Ph.D. degree with the Laboratoire de Conception et d'Intégration des Systèmes, Univ. Grenoble Alpes, Valence, France. His research interests include antenna characterization, antenna array characterization, reverberant chambers, RF circuits, and chipless RFID millimeter- and submillimeter-wave applications.

Romain Siragusa was born in Paris, France. He received the Engineering degree and the Master's degree from the Institute National Polytechnique de Grenoble (Grenoble-INP), Grenoble, France, in 2006, and the Ph.D. degree from the same institute at the Laboratoire de Conception et d'Intégration des Systèmes (LCIS), Valence, France, in 2009, all in electronic engineering. From 2009 to 2010, he joined the "Commissariat À L'énergie Atomique" (CEA) as a Post Doctoral Fellow, where he studied the high impedance surface for integrated antenna on silicon. Since 2011, he has been an Associate Professor with Grenoble-INP Esisar/LCIS. His research interests include leaky-wave structures and chipless radio-frequency identification (RFID).

Nicolas Barbot received the M.Sc. degree and Ph.D. degree in 2010 and 2013 respectively from the University de Limoges, France. His Ph.D. work in Xlim Laboratory was focused on error-correcting codes for the optical wireless channel. He also realized a post-doctoral work in joint source-channel decoding at L2S Laboratory, in Gif-sur-Yvette, France. Since September 2014, he is an Assistant Professor at the Université Grenoble Alpes - Grenoble Institute of Technology, in Valence, France. His scientific background at LCIS Laboratory covers wireless communications systems based on backscattering principle which include classical RFID and chipless RFID. His research interests include transponders which can not be described by linear time-invariant systems. This gathers harmonic transponders which are based on the use of a non-linear component (Schottky diode) or linear time-variant transponders which are based on the modification of their response in the time domain. He also places special interests on antenna design and instrumentation based on these phenomenons.

Etienne Perret (S'02–M'06–SM'13) received the Eng. Dipl. degree in electrical engineering from the Ecole Nationale Supérieure d'Electronique, d'Electrotechnique, d'Informatique, d'Hydraulique, et des Télécommunications, Toulouse, France, 2002, and the M.Sc. and Ph.D. degrees in electrical engineering from the Toulouse Institute of Technology, Toulouse, in 2002 and 2005, respectively. From 2005 to 2006, he held a post-doctoral position with the Institute of Fundamental Electronics, Orsay, France. He was appointed Associate Professor in 2006 and full Professor in 2022 of electrical engineering at Univ. Grenoble Alpes, Grenoble INP, France, where he heads the ORSYS Research Group (20 researchers) from 2015 to 2022. From 2014 to 2019, he has been a Junior Member with the Institut Universitaire de France, Paris, France, an institution that distinguishes professors for their research excellence, as evidenced by their international recognition. From 2015 to 2020, he has been an appointed Member of the French National Council of Universities. He has authored or co-authored more than 200 technical conferences, letters and journal papers, and books and book chapters. He holds several patents. His works have generated more than 3500 citations. His current research interests include wireless communication systems based on the principle of backscatter modulation or backscattering of EM waves especially in the field of RFID and chipless RFID for identification and sensors. His research interests also include electromagnetic modeling of passive devices for millimeter and submillimeter-wave applications, and advanced computer-aided design techniques based on the development of an automated codesign synthesis computational approach. Dr. Perret has been a Technical Program Committee member of the IEEE International Conference on RFID, the IEEE RFID TA; and currently he is a member of the IMS Technical Paper Review Committee. He was a recipient of several awards like the MIT Technology Review's French Innovator's under 35 in 2013, the French Innovative Techniques for the Environment Award in 2013, the SEE/IEEE Leon Brillouin Award for his outstanding achievement in the identification of an object in an unknown environment using a chipless label or tag in 2016, the IEEE MTT-S 2019 Outstanding Young Engineer Award, the Prix Espoir IMT – Académie des sciences in 2020 and the Grand Prix de l'Electronique Général Ferrié in 2021. He was a Keynote Speaker and the Chairman of several international symposiums. Etienne Perret was awarded an ERC Consolidator Grant in 2017 for his project ScattererID.